Analysis of small-scale topology and macroscale mechanical properties of shape memory chiral-lattice metamaterials

Wei Zhao [a], Jie Zhu [a], Liwu Liu [a], Jinsong Leng [b], Yanju Liu [a],*

[a] Department of Astronautical Science and Mechanics, Harbin Institute of Technology (HIT), P.O. Box 301, No. 92 West Dazhi Street, Harbin 150001, People's Republic of China
[b] National Key Laboratory of Science and Technology on Advanced Composites in Special Environments, Harbin Institute of Technology (HIT), P.O. Box 3011, No. 2 YiKuang Street, Harbin 150080, People's Republic of China

ARTICLE INFO

ABSTRACT

Chiral-lattice metamaterials with unique mechanical, optical, electrical and magnetic properties have been widely used in many engineering applications, such as chiral recognition and separation, stealth materials and devices, as well as biological sensors. Various design strategies have been developed to obtain chiral-lattice metamaterials with different mechanical properties. The fast grown design strategies that can provide a variety of Poisson's ratios and elastic moduli have brought new opportunities to emerging biomedical applications. In this study, hexagonal and tetragonal chiral-lattice metamaterials with positive and negative Poisson's ratios were designed. The design strategy was based on a network structure with a periodic lattice topology, which was formed by three outer rings connected to the central ring via ligaments. The wide applications of this type of metamaterial were investigated via experiments and finite-element analysis. Demonstrative examples and the shape-memory effect (SME) suggest that the chiral-lattice structure has great potential in developing programmable metamaterials. The findings of this study provide essential guidance for the design of chiral network structures with the desired mechanical properties.

1. Introduction

In recent years, mechanical metamaterials have emerged as an exciting paradigm and been used for the development of structures with abnormal mechanical properties [1–3]. These structures exhibit advanced functions at the macroscale scale because of their rationally-designed nano/microstructures [3,4]. Their unique unusual properties, such as negative Poisson's ratio, elasticity, and compressibility, can be used to develop advanced functional materials for applications in soft robotics, flexible electronics, acoustic stealth, and other fields [5–11].

The term "metamaterials" originally refers to materials with unusual mechanical properties used in electromagnetism. However, today, all structures or materials designed to have new functions that are not normally found in nature can be called metamaterials [12–14]. Recent achievements in 3D printing technology have made it possible to fabricate structures with complex nanoscale/microstructures and promote the design and manufacture of mechanical metamaterials [15–17]. Consequently, it is very important to thoroughly investigate the relationship between the microscopic topological structure and the macroscopic mechanical properties of mechanical metamaterials to obtain optimum functionality.

Chiral-lattice structures are among the most widely studied mechanical metamaterials. "Chirality" refers to the case where an object does not coincide with its mirror image after operations such as translation and rotation [18–20]. Many biological and manmade materials have a chiral morphology or microstructure, even a multi-level chiral microstructure [20–22]. Moreover, chirality is an important issue in many subjects of natural science, including physics, biology, chemistry, and optics. Chiral microstructures can not only intelligently regulate the growth morphology and color of biomaterials but also determine the physical and mechanical properties (even the biological functions) of biomaterials to a large extent. The chiral microstructure endows a material with chiral symmetry, resulting in the coupling of physical fields such as force-electric and optical-electric, as well as the coupling of mechanical deformations including tension–torsion and bending-shear.

A central circle encased in tangentially connected ligaments constitutes a chiral unit, and it cannot be superimposed on its mirror image [23–25]. Further, the basic unit may be constructed as of right- or left-

handed to form a chiral or backhanded metamaterial, respectively. According to the geometric characteristics of the structures, chiral-lattice metamaterial with a negative or positive Poisson's ratio can be constructed. Under the action of a tension or compression mechanical load, the ligaments rotate, bend, fold, or unfold separately [26–28].

Because of the stretch-torsion coupling effect of chiral-lattice structures and the multiple degrees of freedom, such as translation, rotation, and micro-rotation, micropolar theories were proposed to describe chiral-lattice metamaterials. By introducing three chiral parameters, Lakes et al. established the non-centrosymmetric constitutive relationship of the micro-polarity and investigated the effects of the chirality on the structure and mechanical properties of the material [29]. Papanicolopulos et al. proposed a strain gradient theory to investigate the mechanical behavior of a chiral material, where only one parameter was introduced [30]. Helfrich examined the bending force of chiral molecular films and found that the chiral correlation term in the expression of the bending energy of the film was related to the direction of cylindrical curvature [31]. According to the micropolar theory, Joumaa et al. investigated the stress invariance of chiral microporous material models in the in-plane and anti-plane problems [32]. Wang et al. proposed the Euler-Bernoulli model with surface effects and chirality, which was used to study the buckling of chiral structures [33].

For chiral-lattice structures, most of the previous studies were theoretical studies; few experimental studies have been performed to reveal their mechanical properties, such as Poisson's ratio and elastic modulus. Furthermore, theoretical research on micropolar behavior is generally based on the assumption of rigid rings, which is difficult to achieve under real conditions. Thus, in the present study, through the analysis of the mechanical behavior of chiral structures, two types of chiral-lattice structures (hexagonal and tetragonal, with positive and negative Poisson's ratios, respectively) were designed. Subsequently, utilizing the shape memory polymer (SMP) based filament, the chiral-lattice metamaterials are fabricated via 3D printing. Both lattices had the characteristics of internal rotating elements, which are connected by tangential ligaments of joints in a circular form.

The mechanical properties of chiral-lattice metamaterials associated with different topological parameters were thoroughly investigated. The Poisson's ratio (ν) and elastic modulus were determined via experiments and finite-element analysis (FEA). Finally, three-dimensional (3D) assembly cylinder shells were proposed according to the developed two-dimensional (2D) chiral lattice networks. By utilizing the shape memory effect, chiral-lattice metamaterials can be programmed with different shapes [34–43]. Interestingly, the reshaped metamaterials can show mechanical behaviors that differ from the original structures. To our knowledge, this is the first thorough characterization of the mechanical properties of the chiral-lattice metamaterials changing with respect to the topological parameters via detailed experiments and FEA.

2. Design, experiments, and finite element analysis

2.1. Design

2.1.1. Hexagonal chiral lattice

The structure of the hexagonal chiral lattice is shown in Fig. 1. The representative triangular volume element consists of four circles (as joints): three outer rings, and one central ring. Each outer ring is connected with the central ring by ligaments, which is tangential to the two rings. The angles between the ligament and connecting lines (between the two rings' center) are denoted as θ_a. The side length of the imaginary equilateral (Fig. 1(a)) is a, the radius of the central ring (with a wall thickness of t_R) is R, the radius of the other three outer rings (with a wall thickness of t_r) is r, and the length of the ligament
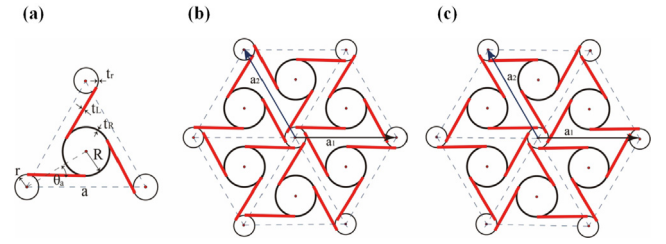

Fig. 1. Geometric configurations of hexagonal chiral-lattice structure. (a) Representative unit-cell and the definition of the geometric parameters. (b) Left-handed lattice metamaterials. (c) Right-handed lattice metamaterials.

is L (with a width of t_L). According to the geometric characteristics, the following relation can be drawn: $\sin\theta_a = \frac{\sqrt{3}(r+R)}{3a}$ and $\cos\theta_a = \frac{\sqrt{3}L}{a}$. The lattice structure illustrated in Fig. 1(b) can be obtained by arranging the representative unit-cell along the symmetric vectors α_1 and α_2. The vector is one of the possible sets to realize the symmetrical hexagon, which can be expressed as follows:

$$\alpha_2 = -\frac{1}{2}ai_1 + \frac{\sqrt{3}}{2}ai_2 \tag{1}$$

From the previously mentioned geometric relationship, we can obtain $R + r = \frac{\sqrt{3}}{3}a\sin\theta_\alpha$ and $L = \frac{\sqrt{3}}{3}a\cos\theta_\alpha$. Here, a topological parameter q is defined, which satisfies the following relations:

$$R = (1-q)\frac{\sqrt{3}}{3}a\sin\theta_\alpha, r = q\frac{\sqrt{3}}{3}a\sin\theta_\alpha, q \in [0, 1], \theta_\alpha \in [-90°, 90°] \tag{2}$$

By changing the value of q, the diameters of the outer rings and central ring can be adjusted. Meanwhile, the value of q is directly related to the chirality of the chiral-lattice metamaterials. Furthermore, the topology angles $\theta_\alpha \in [-90°, 90°]$ can also significantly affect the mechanical behavior and geometric configuration of chiral-lattice metamaterials. When $\theta_\alpha \to 0$, the ring degenerates to a point, and the conventional square lattice structures are obtained. When $\theta_a \to \pm 90°$, the ligament completely vanishes, and the whole lattice is only composed of rings. In either case, the chirality will disappear, because it is caused by the bending and the winding of the ligament.

The geometric configurations of the unit-cell changing with the topological angles are shown in Fig. 2

2.1.2. Tetragonal chiral lattice

The layout of the tetragonal chiral lattice is shown in Fig. 3. In each equilateral quadrilateral element with a side length of a, an inner ring with radius R is connected with each one of four outer rings with radii r by a tangential ligament with length L, as shown in Fig. 3(a). The wall thicknesses of the ligament, the outer rings, and the inner rings of the imaginary tetrahedron are denoted as t_L, t_r, and t_R, respectively.

The ratio of length L to thickness t_L of the ligaments is defined as $x_L = t_L/L$, and the ratio of the thickness t_R to the radius R of the rings is defined as $x_R = t_R/R$. The geometric parameters have the following
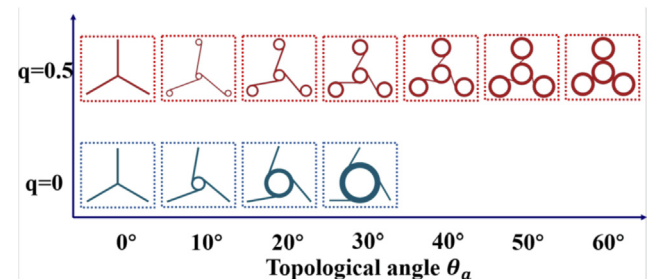

Fig. 2. The unit element of the hexagonal chiral lattice with different θ_a.
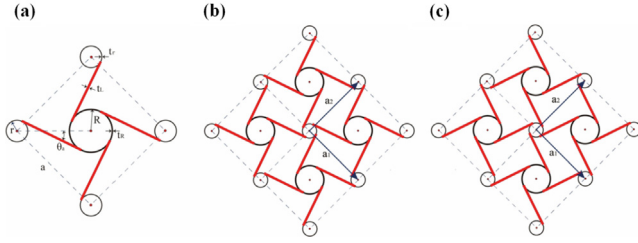
Fig. 3. Geometric configurations of the tetragonal chiral lattice. (a) The basic element and definition of the topological parameters. (b) Left-handed lattice structures. (c) Right-handed lattice structures.

relations:$\sin\theta_\alpha = \frac{\sqrt{2}(r+R)}{a}$ and $\cos\theta_\alpha = \frac{\sqrt{2}L}{a}$. The vectors α_1 and α_2 are one of the possible sets of the unit-cell for obtaining the symmetrical tetragonal chiral lattice, which can be expressed as follows:

$$\alpha_1 = -\frac{\sqrt{2}}{2}a\,i_1 + \frac{\sqrt{2}}{2}a\,i_2, \alpha_2 = \frac{\sqrt{2}}{2}a\,i_1 + \frac{\sqrt{2}}{2}a\,i_2 \qquad (3)$$

The radii of the rings in Fig. 3 satisfy the relation $R + r = \frac{\sqrt{2}}{2}a\sin\theta_\alpha$ and $L = \frac{\sqrt{2}}{2}a\cos\theta_\alpha$. According to the geometric relation, R and r can be expressed as follows:

$$R = q\frac{\sqrt{2}}{2}a\sin\theta_\alpha, r = (1-q)\frac{\sqrt{2}}{2}a\sin\theta_\alpha, q\in[0,1]\theta_\alpha\in[-90°,\ 90°] \qquad (4)$$

The geometric configurations of the chiral lattices changing with the topological parameters θ_α are shown in Fig. 4.

2.1.3. Fabrication

The samples of chiral-lattice metamaterials with 74 in total (hexagonal and tetragonal chiral lattices) were fabricated by 3D printing to investigate the mechanical properties with different topological parameters θ_α, x_R, x_L, and q. Details regarding the design parameters of the samples are presented in the Supporting Information S1.

The chiral-lattice metamaterials samples are made of shape memory polylactic acid (SMP-PLA) by 3D printing. The SMP-PLA filament is provided by the National Key Laboratory of Science and Technology on Advanced Composites in Special Environments (Harbin Institute of Technology). An ANYCUBIC commercial 3D printer (i3 MEGA) with a nozzle size of 0.4 mm was employed to fabricate the samples. The printing speed was set as 50 mm/min, the printing temperature was 210 ℃, the bed temperature was 60 ℃, and the filling density is 20%. The mechanical properties of the SMP-PLA are presented in Fig. S8, Supporting Information S6.

2.2. Experiments

2.2.1. The measurement of mechanical properties

The mechanical properties of the chiral-lattice metamaterials were tested using a Zwick/Rolle-010 universal testing machine, and the
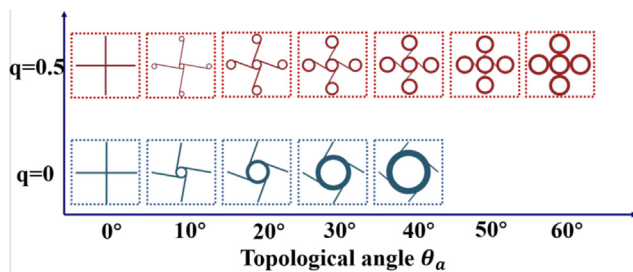
stress–strain curves with a loading rate of 2 mm/min were recorded. During this process, the Poisson's ratio was determined via the template-matching method, which was a visual target tracking technology [44]. By using this method, the changes in the transversal and longitudinal displacements can be captured. It involved identifying the region in the original image with the highest matching degree with the template image. During the loading process, the movements of the points A, B, A', and B' marked in Fig. 5 were recorded by a camera. Given the original image I and the template image T, the motion rules could be captured when the template matching operation was performed for each video frame. Additionally, the normalized correlation coefficient matching method was adopted for image matching to improve the tracking accuracy. Using this method, the region with the highest matching degree was calculated directly. Additional details regarding the calculations of the Poisson's ratio are presented in Supporting Information S3.

2.2.2. The measurement of shape memory behavior

A typical shape-memory process consists of two stages: shape programming and shape recovery. First, the chiral lattices were heated to 70 ℃ and stabilized for 2 min. 18% deformation was applied with a loading rate of 2 mm/min (Step 1). Subsequently, the deformation was kept constant, and the temperature was decreased to 20 ℃ at a cooling rate of 2 ℃/min. The programmed shape was memorized after the cooling process, and the mechanical load was removed (Steps 2 and 3). Finally, the chiral-lattice metamaterials were reheated to recover to their initial shape (Step 4). Exemplified by the hexagonal and tetragonal chiral-lattice metamaterials with $\theta_\alpha = 20°$, the shape memory behavior was measured using a Zwick/Rolle-010.

2.3. Finite element analysis

According to the micropolar theory, the ring elements are assumed to be rigid, which neglects the strain energy related to ring deformation. However, the hypothesis of the rigid ring is difficult to realize with practical fabrication techniques. Generally, the deformation of chiral-lattice metamaterials with deformable rings is difficult to describe. Even a reasonable ring model is constructed based on too many approximate representations of the linear component, or nonlinear coupling equations of curved beams. It is still challenging to obtain an analytic solution.

For this reason, finite element analysis (FEA) is carried out to reveal the mechanical behavior of chiral-lattice metamaterials in this research. The overall deformation of the chiral lattice comprises both ligament bending and ring stretching. Any change in a topological
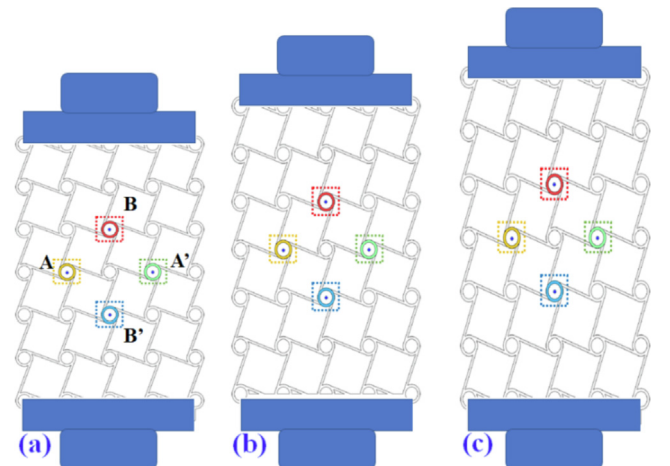

Fig. 4. Geometric configurations of the tetragonal chiral lattice with different topological angles θ_α.

Fig. 5. Schematic of the method for determining the Poisson's ratio.

parameter will break the balance among those parameters and affect the mechanical behavior of the structures. When the ring stiffness increases under a constant deformation condition, the ligament bending deformation increases proportionally; otherwise, it will decrease.

Simulations of the large deformation and thermal–mechanical cycle of the chiral-lattice metamaterials were performed using the commercial finite-element software Abaqus (version 6.14, 3DS Dassault Systèmes, France). The chiral-lattice metamaterials models were built and meshed with linear hexahedral elements of type C3D8R. The shift function was defined by user subroutine UTRS, and the time-domain viscoelasticity was defined by the expansion of the Prony series (Notes S5, Supporting Information). The related model parameters were determined via a series of experiments and presented in Table S8. The deformation sequences of chiral-lattice metamaterials and the unit-cell are shown in Fig. 6.

3. Results and discussions

3.1. Shape-memory behavior

The recorded thermal–mechanical cycle curves are shown in Fig. 7 (a), and the programmed and recovered states of chiral-lattice metamaterials composed of units with $\theta_\alpha = 20°$ are shown in Fig. 7(b) and (c). The hexagonal and tetragonal chiral-lattice metamaterials are applied 18% stretched and 18% compressed deformation, respectively. By utilizing this process, metamaterials can be programmed to a specific configuration through controlling the strain ε, and the programmed and recovered states can switch each other under certain stimuli. Based on the shape memory effect, the Poisson's ratio and elastic modulus can be adjusted.

3.2. Mechanical deformation and Poisson's ratio

Hexagonal lattice metamaterials are characterized by hexagonal symmetry because each node has six tangentially connected ligaments. The rings enhance the resistance to out-of-plane bucking and compressive strength of the structure. The deformation mechanism of the chiral lattice is closely related to the topological parameters. As the topological angle θ_α decreases, the deformation mechanism of the chiral-lattice structure changes from the stretching-dominant to bending-dominant behavior.
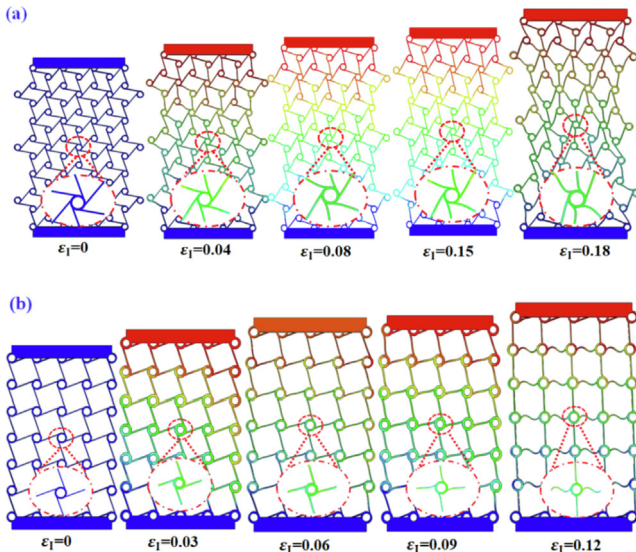

Fig. 6. Deformation sequences of the network: (a) Hexagonal chiral lattice; (b) Tetragonal chiral lattice.

In this study, a series of chiral-lattice metamaterials with different topological angles θ_α were designed (Table S1, Supporting Information S1) to investigate the effects of the topological parameters on the Poisson's ratio, as shown in Fig. 8. For the chiral-lattice metamaterials with $x_L = 0.05$, with the increase of the topological angle θ_α, the Poisson's ratio increased gradually (Table 1). According to the recorded video, the chirality behavior was relatively obvious for topological angles ranging from $\theta_\alpha = 20°$ to $\theta_\alpha = 40°$. When the rings were too small or too large, no chirality was observed. However, it is worth mentioning that the rings and ligaments are almost jointed together when $\theta_\alpha = 60°$ and no chirality behavior can be observed.

For tetragonal chiral-lattice metamaterials (Table S2, Supporting Information S1), the Poisson's ratios were negative in the small-deformation case (Table 1). However, with the increase of θ_α, no obvious regularity can be observed for either small or large deformation, as shown in Fig. 9. Additionally, the absolute value of ν for the chiral structure with $x_L = 0.1$ was significantly smaller than that of the structures with $x_L = 0.05$. As mentioned above, the negative Poisson's ratio was caused by the bending and winding of the ligament. However, the increasing ligament stiffness limited the deformation of ligaments and further resulted in the decrease of the Poisson's ratio. According to the recorded video, the chirality behavior was evident when the topological angle ranged from $\theta_\alpha = 20°$ to $\theta_\alpha = 40°$, and it had lost the chirality behavior when $\theta_\alpha = 60°$.

The Poisson's ratios of hexagonal chiral lattices with $q = 0$ (Supporting Information S1, Table S3) were also investigated, as shown in Fig. 10. Similar to the chiral-lattice metamaterials with $q = 0.5$, the Poisson's ratio decreased with the increase of the topological angle θ_α (Table 2). The chiral behavior was obvious to be observed when the topological angle θ_α ranges from $\theta_\alpha = 10°$ to $\theta_\alpha = 20°$. However, for the chiral lattice with $\theta_\alpha = 25°$, the Poisson's ratio changed abnormally. Proved by the experiments and finite element analyses, the hexagonal chiral lattices have lost the chirality behavior when $\theta_\alpha = 30°$.

The topological parameter x_R has a direct impact on the ring stiffness and further affects the overall deformation of the structure. A series of chiral-lattice metamaterials with different topological parameters x_R were designed to investigate the effect on the mechanical properties (Supporting Information S1, Tables S4, and S5).

For tetragonal chiral lattice, with the increase of the rings' stiffness, the deformation contributed by it decreased gradually, and the ligament bending played a leading role in the deformation. Therefore, the absolute value of ν increased with the increasing x_R. As shown in Fig. 11, the Poisson's ratio of the tetragonal chiral lattice was $\nu = -0.68$ with $x_R = 0.02$ and $\nu = -0.94$ with $x_R = 0.10$. However, for the hexagonal chiral lattice, no obvious change rule was observed about the Poisson's ratio except for $x_R = 0.08$, $x_R = 0.09$, and $x_R = 0.10$. The changes of the Poisson's ratio were irregular, potentially owing to the complex structural changes of the six ligaments.

Chiral-lattice metamaterials with different topological parameters x_L were also designed to investigate the effect of x_L on the mechanical properties (Supporting Information S1, Table S6 and S7). The absolute value of Poisson's ratios ($x_L = 0.05$, $x_L = 0.06$, $x_L = 0.08$, and $x_L = 0.10$) decreased gradually with the increase of x_L, as shown in Fig. 12 (b). However, when $x_L = 0.025$, $x_L = 0.03$, $x_L = 0.04$, $x_L = 0.15$ and $x_L = 0.20$, the Poisson's ratio changed irregularly. This could be because, with the increase of the rings' stiffness, the structural deformation gradually changed from ligament bending-dominated to ring stretching-dominated deformation.

3.3. Determination of elastic moduli

The topological parameters not only significantly affected the Poisson's ratios of the chiral-lattice metamaterials but also had a signifi-
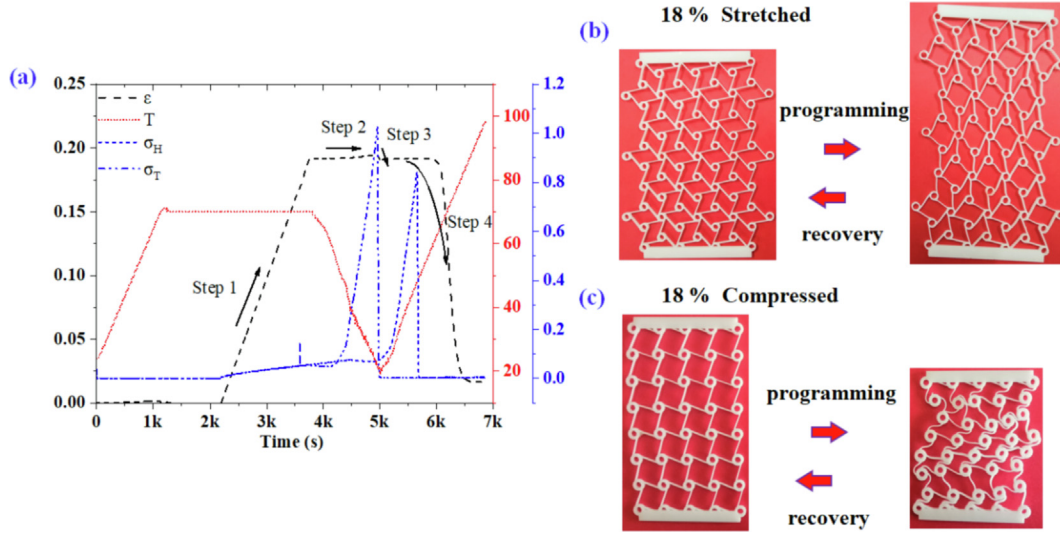
Fig. 7. Shape memory cycles for chiral-lattice metamaterials: (a) Thermo-mechanical cycle curves; (b) Hexagonal chiral-lattice metamaterials with $\theta_\alpha = 20°$; (c) Tetragonal chiral-lattice metamaterials with $\theta_\alpha = 20°$.
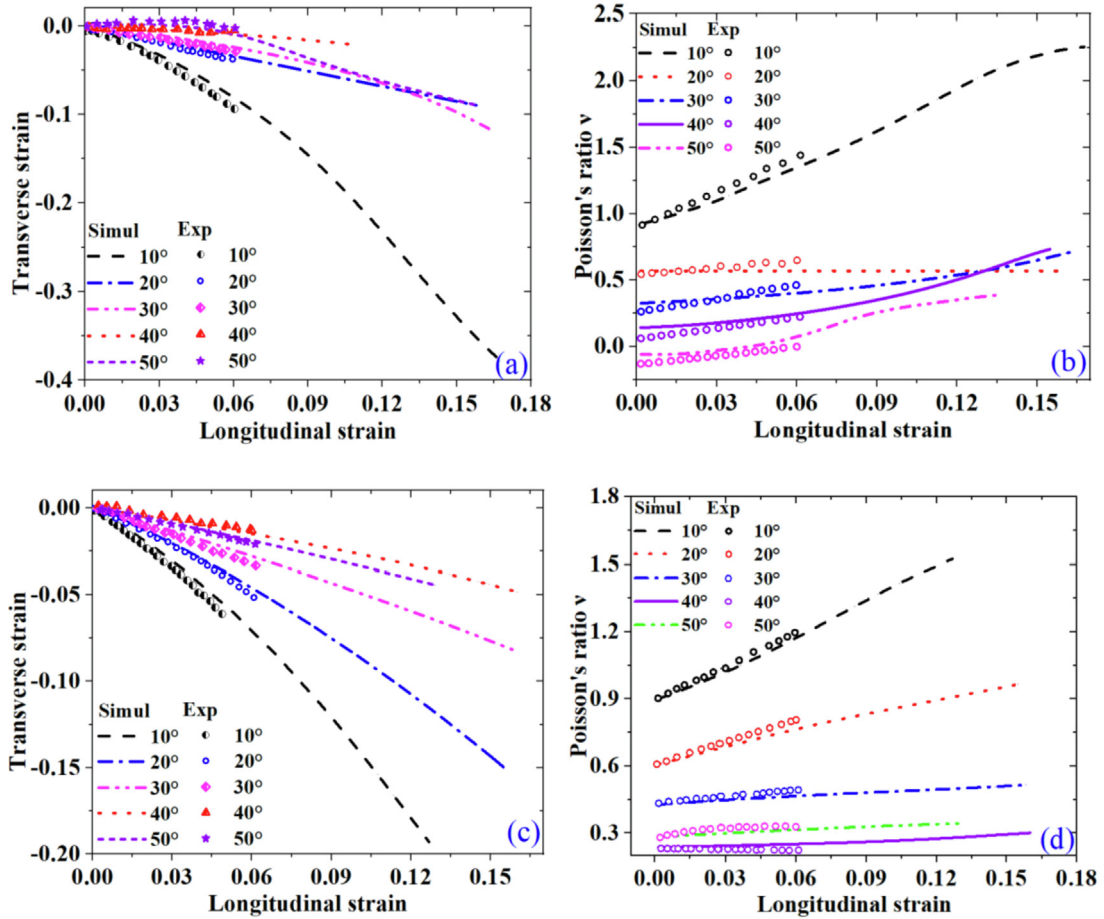

Fig. 8. Comparisons between the simulated results and experimental results for the hexagonal chiral lattice with different topological angles θ_α and $q = 0.5$. (a) Transverse strain vs. longitudinal strain with $x_L = 0.05$. (b) Poisson's ratio ν with $x_L = 0.05$. (c) Transverse strain vs. longitudinal strain with $x_L = 0.1$. (d) Poisson's ratio ν with $x_L = 0.1$.

Table 1
The Poisson's ratio of the chiral-lattice metamaterials with $q = 0.5$ in the small-deformation case.

	Hexagonal chiral lattice		Tetragonal chiral lattice	
	$x_L = 0.05$	$x_L = 0.1$	$x_L = 0.05$	$x_L = 0.1$
$\theta_\alpha = 10°$	0.94	0.90	-0.86	-0.38
$\theta_\alpha = 20°$	0.56	0.61	-0.68	$-0.41,$
$\theta_\alpha = 30°$	0.33	0.43	-0.55	-0.11
$\theta_\alpha = 40°$	0.14	0.23	-0.36	-0.16
$\theta_\alpha = 50°$	-0.06	0.29	-0.30	-0.20
$\theta_\alpha = 60°$			-0.31	0.78

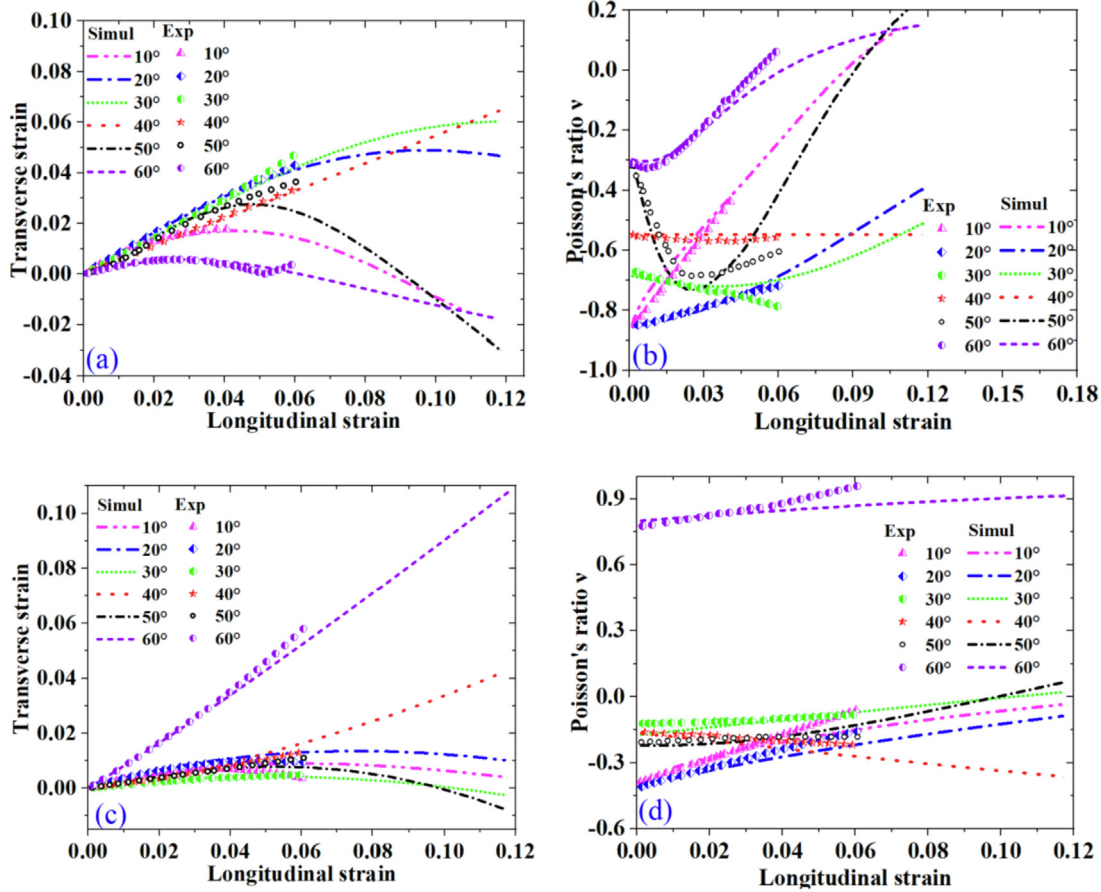**Fig. 9.** Comparisons between the simulated and experimental results for the tetragonal chiral-lattice with different topological angles θ_α and $q = 0.5$. (a) Transverse strain vs. longitudinal strain with $x_L = 0.05$, (b) Poisson's ratio ν with $x_L = 0.05$, (c) transverse strain vs. longitudinal strain with $x_L = 0.1$, and (d) Poisson's ratio ν with $x_L = 0.1$.

cant influence on the stiffness of the structures. By using the obtained nominal stress-nominal strain curves (Supporting Information S2), the equivalent elastic moduli of the structures were calculated and compared with the simulated results (Fig. 13).

From the results, it can be observed that when $\theta_\alpha < 40°$, the deformation mode was still bending-dominated. Consequently, the increase of the equivalent elastic modulus is not significant about the chiral lattice with $\theta_\alpha = 10°$, $\theta_\alpha = 20°$, and $\theta_\alpha = 30°$. However, when $\theta_\alpha \geqslant 40°$, the stretching deformation of the rings gradually paly a leading role, and the elastic moduli increase dramatically.

The equivalent elastic moduli of the chiral-lattice metamaterials ($\theta_\alpha = 30°$) with different topological parameters x_R are presented in Fig. 14. According to the simulated and experimental results, the

equivalent elastic moduli did not change significantly with the increase of x_R. As mentioned above, the deformation mode was bending dominated when $\theta_\alpha = 30°$. Consequently, it can be concluded that in the bending-dominated deformation mode, the change in the ring stiffness was not decisive to the equivalent elastic moduli.

The equivalent elastic moduli of metamaterials ($\theta_\alpha = 30°$) with different topological parameters x_L are presented in Fig. 15. According to the experimental and simulated results, the equivalent elastic moduli of the hexagonal chiral lattice changed slightly at $x_L \leqslant 0.08$. However, when $x_L > 0.08$, the deformation mechanism changed from bending-dominated to tensile-dominated. Consequently, the equivalent elastic moduli increased dramatically. For the tetragonal chiral lattice, the equivalent elastic moduli started to change dramatically at $x_L = 0.05$.
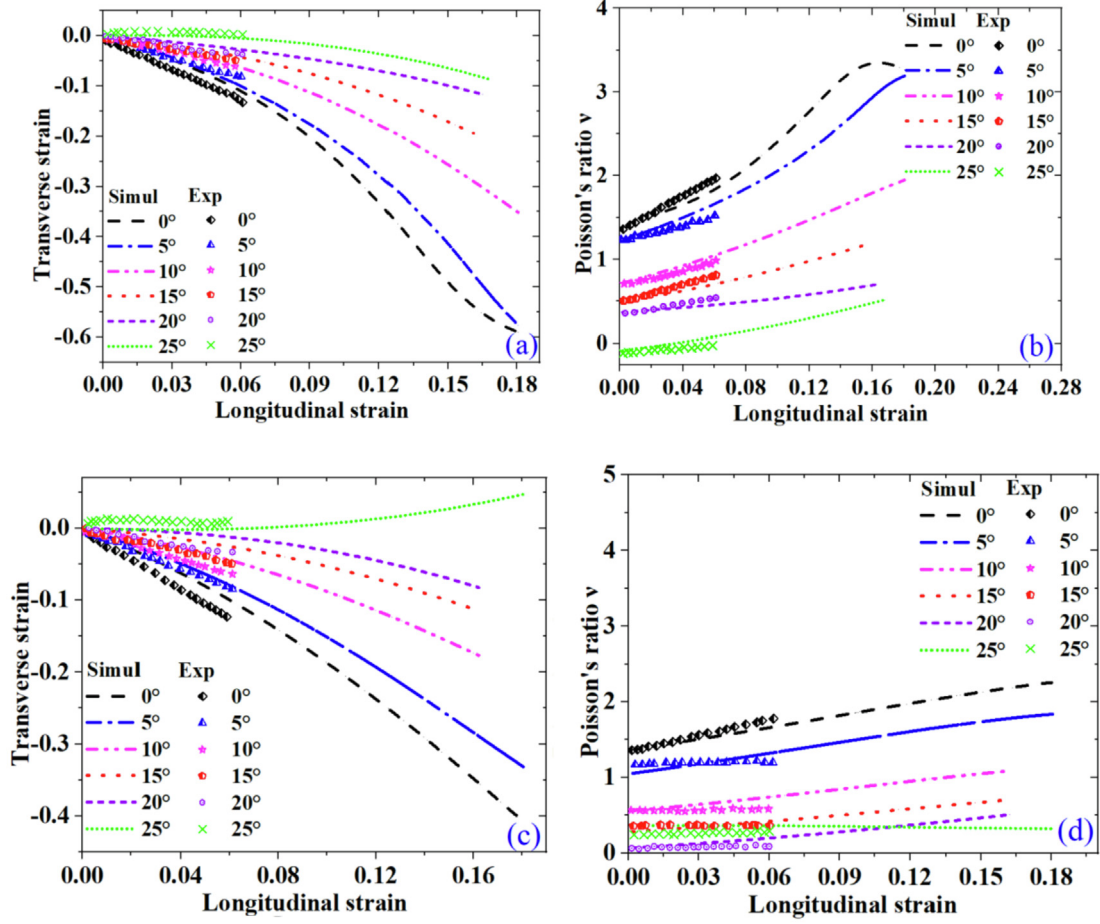
Fig. 10. Comparisons between the simulated and experimental results for the hexagonal chiral lattice with different topological angles θ_α and $q = 0$ (a) Transverse strain vs. longitudinal strain with $x_L = 0.05$; (b) Poisson's ratio ν with $x_L = 0.05$; (c) transverse strain vs. longitudinal strain with $x_L = 0.1$; (d) Poisson's ratio ν with $x_L = 0.1$.

Table 2
The Poisson's ratio of the chiral-lattice metamaterials with $q = 0$ in the small-deformation case.

	Hexagonal chiral lattice	
	$x_L = 0.05$	$x_L = 0.1$
$\theta_\alpha = 0°$	1.38	1.33
$\theta_\alpha = 5°$	1.25	1.06
$\theta_\alpha = 10°$	0.70	0.59
$\theta_\alpha = 15°$	0.51	0.37
$\theta_\alpha = 20°$	0.35	0.06
$\theta_\alpha = 25°$	-0.07	0.23

For the chiral-lattice structures with $q = 0$, the simulated and experimental results for the equivalent elastic moduli are shown in Fig. 16.

3.4. Deformation of the assembly cylinder shell

A series of cylinder metamaterials were designed and fabricated according to the proposed 2D chiral lattices. The metamaterials cylinder structures were composed of the hexagonal, tetragonal chiral lattices, and their combinations, as shown in Fig. 17 (a)–(c). The unit
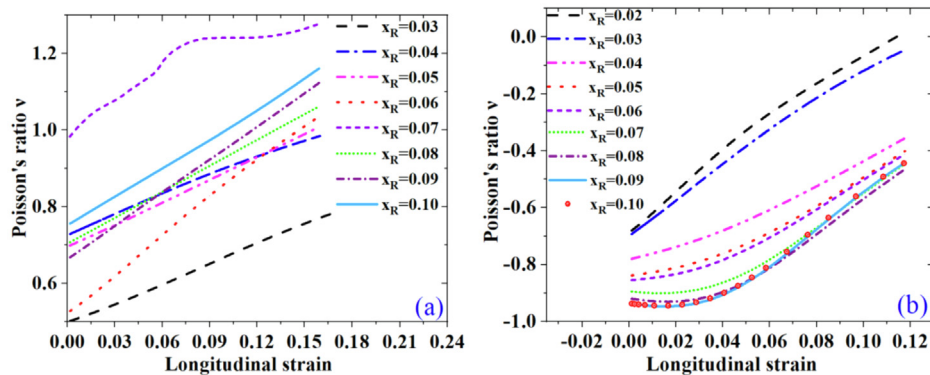

Fig. 11. Effect of the topological parameter x_R on the Poisson's ratio for (a) the hexagonal chiral lattice and (b) the tetragonal chiral lattice.
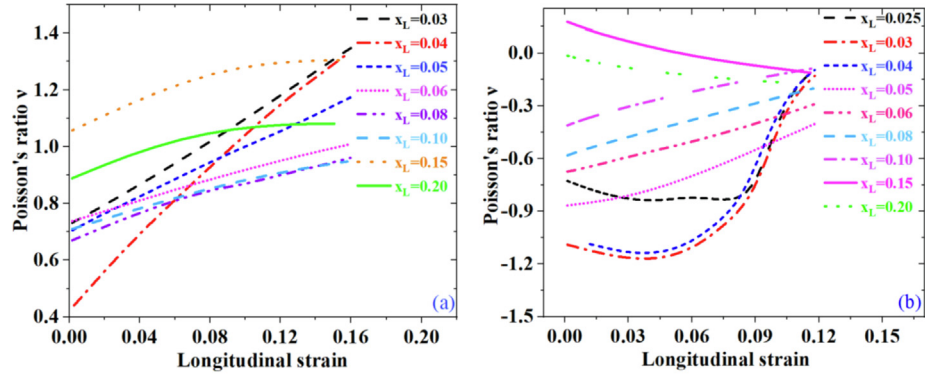
Fig. 12. Effect of x_L on the Poisson's ratio for the (a) hexagonal chiral lattice and (b) tetragonal chiral lattice.
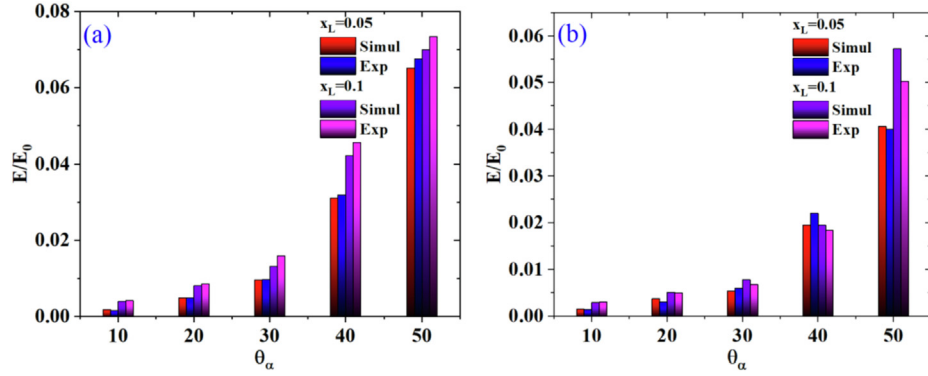

Fig. 13. Equivalent elastic moduli of metamaterials with different topological angles (θ_α) for the (a) hexagonal chiral lattice and (b) tetragonal chiral lattice. (The equivalent elastic moduli of the chiral structures were denoted as E, and the elastic modulus of the SMP-PLA was $E_0 = 1850$ MPa).
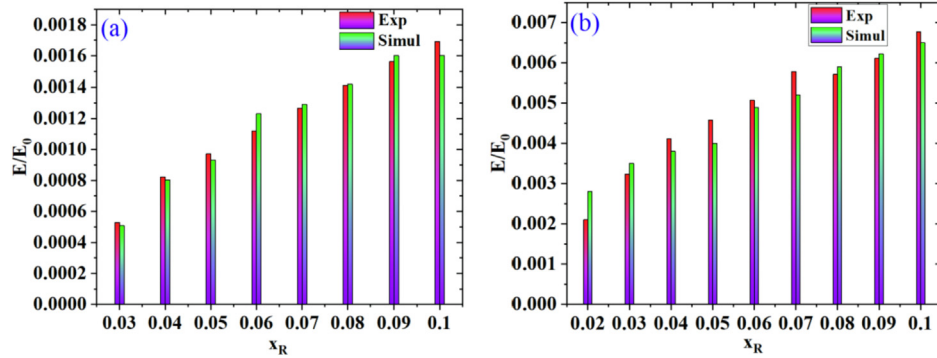

Fig. 14. Equivalent elastic moduli of metamaterials with different topological parameter (x_R) for the (a) hexagonal chiral lattice and (b) tetragonal chiral lattice.
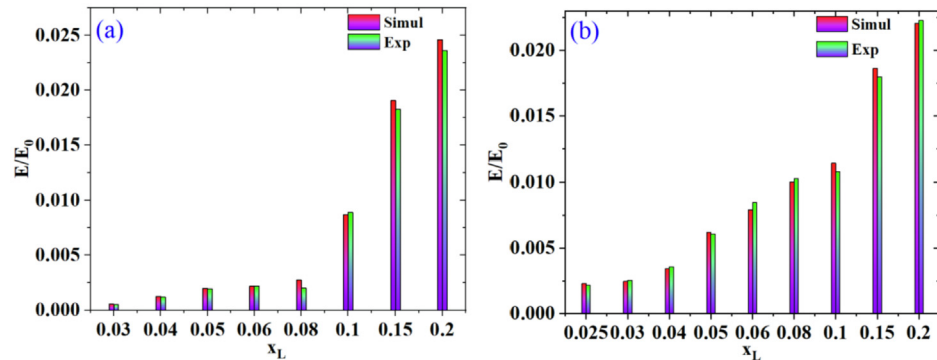

Fig. 15. Equivalent elastic moduli of metamaterials with different topological parameters (x_L) for the (a) hexagonal chiral lattice and (b) tetragonal chiral lattice.
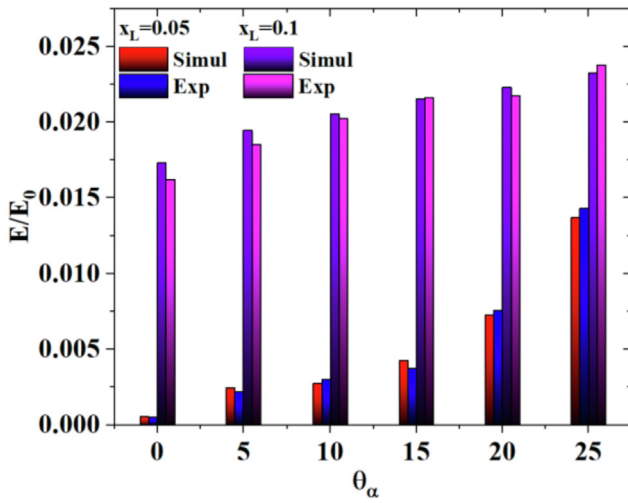
Fig. 16. Equivalent elastic moduli of metamaterials with different topological parameters (x_L) and $q = 0$ for the (a) hexagonal chiral lattice and (b) tetragonal chiral lattice.
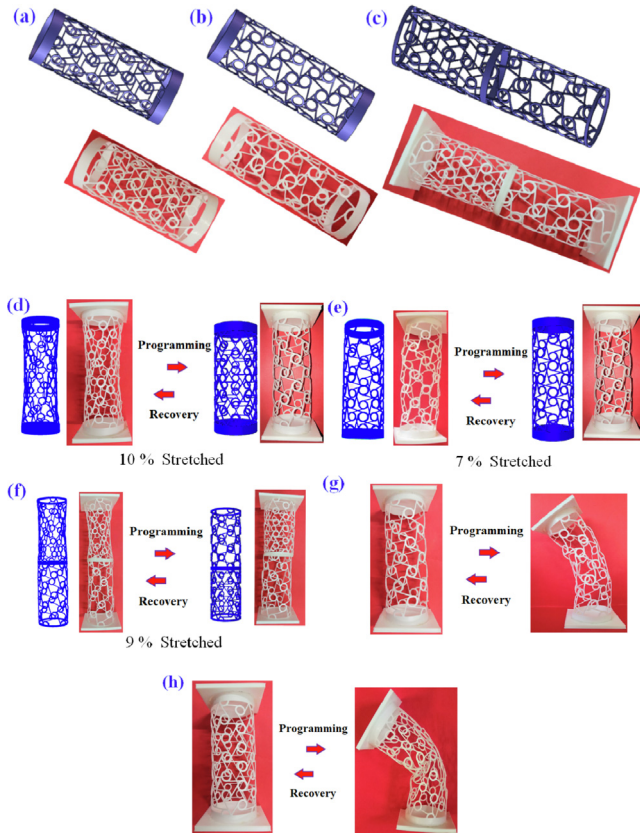

Fig. 17. Characterization of the shape memory behavior of the assembly cylinder shell; (a) hexagonal chiral lattice; (b) tetragonal chiral lattice; (c) combination of the hexagonal and tetragonal chiral lattices; simulation and experiment for the (d) hexagonal chiral lattice after 10% stretching, (e) tetragonal chiral lattice after stretching for 7%, and (f) the combination of the two structures after stretching for 10%; The recovered state and programmed state of (g) the tetragonal chiral lattice under bending load, and (h) the hexagonal chiral lattice under bending load.

elements with a topological angle of $\theta_\alpha = 30°$ were used. For the structures shown in Fig. 17(a) and (b), there were four complete unit-cells in the circumferential and axial directions of the cylinder.

For the combination type cylinder, there were three complete elements in the circumferential and axial directions.

One end of the cylinder was fixed, and a certain load was applied on the free end. The programming and recovery process used in the simulation and experiments are shown in Fig. 17(d)–(f). According to the previous result, during the stretching process, the cross-section of the cylinder comprising the hexagonal chiral lattice should shrink gradually, while the cross-section of the cylinder comprising the tetragonal chiral lattice should expand. However, the auxetic behavior for the cylinder comprising the hexagonal chiral lattice is not obvious since the limited number of the unit element.

Under a bending load, the programmed state and the recovered state of the tetragonal chiral lattice and the hexagonal chiral lattice are shown in Fig. 17 (g) and (h). After the programming process, the 3D metamaterials cylinder is fixed to a temporary shape based. Due to the shape memory effect and the programming process, the new configuration is endowed with different mechanical properties. Meanwhile, the programmed shape can be erased during the recovery process. This ensures the metamaterial can be adjusted purposely to any state as required.

4. Conclusions

By controlling topological parameters, a series of new configurations of hexagonal and tetragonal chiral-lattice metamaterials with adjustable Poisson's ratio of (0, 2.3) and (−0.85, 0.2) were designed and fabricated via 3D printing. The effects of the topological parameters θ_α, x_R, x_L, and q on the Poisson's ratio and elastic modulus were thoroughly investigated via FEA and experiments. The results indicated that the mechanical properties, including the Poisson's ratio and elastic modulus, are very sensitive to changes in these topological parameters. Utilizing the 2D chiral lattice networks, metamaterial cylindrical shells were developed, and the shape memory behavior was investigated via FEA and experiments. Being incorporated into shape memory effect, the metamaterials can be programmed into any configuration and endowed with different mechanical properties as required. This can significantly accelerate the design and development period. Furthermore, the programmability provides an opportunity to adjust the mechanical properties of the metamaterials after fabrication. Integrating active functionality into the network and extending the design into three-dimensional structures may facilitate and broaden the applications of metamaterials in active deformation structures.

Declaration of Competing Interest

The authors declare that they have no known competing financial interests or personal relationships that could have appeared to influence the work reported in this paper.

Acknowledgments

Appendix A. Supplementary data

Supplementary data to this article can be found online at https://doi.org/10.1016/j.compstruct.2021.113569.

References

[1] Kolken HM, Zadpoor AA. Auxetic mechanical metamaterials. RSC Adv 2017;7 (9):5111–29.
[2] Nicolaou ZG, Motter AE. Mechanical metamaterials with negative compressibility transitions. Nat Mater 2012;11(7):608–13.

[3] Zadpoor A. Mechanical meta-materials. Mater Horiz 2016;3:371–81.

[4] Lee JH, Singer JP, Thomas EL. Micro-/nanostructured mechanical metamaterials. Adv Mater 2012;24(36):4782–810.

[5] Lei M, Hong W, Zhao Z, Hamel CM, Chen M, Lu HB, et al. 3D printing of auxetic metamaterials with digitally reprogrammable shape. ACS Appl Mater Interfaces 2019;11(25):22768–76.

[6] Huang J, Zhang QH, Scarpa F, Liu YJ, Leng JS. Multi-stiffness topology optimization of zero Poisson's ratio cellular structures. Compos Part B 2018;140:35–43.

[7] Rafsanjani A, Pasini D. Bistable auxetic mechanical metamaterials inspired by ancient geometric motifs. Extreme Mech Lett 2016;9:291–6.

[8] Papadopoulou A, Laucks J, Tibbits S. Auxetic materials in design and architecture. Nat Rev Mater 2017;2:17078.

[9] Wei K, Chen H, Pei Y, Fang D. Planar lattices with tailorable coefficient of thermal expansion and high stiffness based on dual-material triangle unit. J Mech Phys Solids 2016;86:173–91.

[10] Mirzaali MJ, Caracciolo A, Pahlavani H, Janbaz S, Vergani L, Zadpoor AA. Multi-material 3D printed mechanical metamaterials: Rational design of elastic properties through spatial distribution of hard and soft phases. Appl Phys Lett 2018;113:241903.

[11] Li T, Chen Y, Hu X, Li Y, Wang L. Exploiting negative Poisson's ratio to design 3D-printed composites with enhanced mechanical properties. Mater Des 2018;142:247–58.

[12] Cai W, Chettiar UK, Kildishev AV, Shalaev VM. Optical cloaking with metamaterials. Nat Photonics 2007;1(4):224–7.

[13] Shalaev VM. Optical negative-index metamaterials. Nat Photonics 2007;1(1):41–8.

[14] Smith DR, Pendry JB, Wiltshire MC. Metamaterials and negative refractive index. Science 2004;305(5685):788–92.

[15] Yang L, Harrysson O, Cormier D, West D, Gong H, Stucker B. Additive manufacturing of metal cellular structures: design and fabrication. JOM 2015;67(3):608–15.

[16] Zhao W, Zhang FH, Leng JS, Liu YJ. Personalized 4D printing of bioinspired tracheal scaffold concept based on magnetic stimulated shape memory composites. Compos Sci Technol 2019;184:107866.

[17] Akbari S, Sakhaei AH, Kowsari K, Yang B, Serjouei A, Zhang Y, et al. Enhanced multimaterial 4D printing with active hinges. Smart Mater Struct 2018;27(6):065027.

[18] Alderson A, Alderson K, Attard D, Evans K, Gatt R, Grima J, et al. Elastic constants of 3-, 4- and 6-connected chiral and antichiral honeycombs subject to uniaxial in-plane loading. Compos Sci Technol 2010;70(7):1042–8.

[19] Prall D, Lakes R. Properties of a chiral honeycomb with a Poisson's ratio of—1. Int J Mech Sci 1997;39(3):305–14.

[20] Ha S, Plesha ME, Lakes RS. Chiral three-dimensional lattices with tunable Poisson's ratio. Smart Mater Struct 2016;25(5):054005.

[21] Armon S, Efrati E, Kupferman R, Sharon E. Geometry and mechanics in the opening of chiral seed pods. Science 2011;333(6050):1726–30.

[22] Thiemann W. Life and chirality beyond the earth. Origins Life Evol B 1975;6(4):475–81.

[23] Mousanezhad B, Haghpanah R, Ghosh A, Hamouda M, Nayeb-Hashemi H, Vaziri A. Elastic properties of chiral, anti-chiral, and hierarchical honeycombs: a simple energy-based approach. Appl Mech Lett 2016;6(2):81–96.

[24] Spadoni A, Ruzzene M, Scarpa F. Global and local linear buckling behavior of a chiral cellular structure. Phys Status Solidi B 2005;242(3):695–709.

[25] Scarpa F, Blain S, Lew T, Perrott D, Ruzzene M, Yates J. Elastic buckling of hexagonal chiral cell honeycombs. Compos Part A 2007;38(2):280–9.

[26] Abramovitch H, Burgard M, Edery-Azulay L, Evans K, Hoffmeister M, Miller W, et al. Smart tetrachiral and hexachiral honeycomb: sensing and impact detection. Compos Sci Technol 2010;70(7):1072–9.

[27] Gatt R, Brincat JP, Azzopardi KM, Mizzi L, Grima JN. On the effect of the mode of connection between the node and the ligaments in anti-tetrachiral systems. Adv Eng Mater 2015;17(2):189–98.

[28] Huang HH, Wong BL, Chou YC. Design and properties of 3D-printed chiral auxetic metamaterials by reconfigurable connections. Phys Status Solidi B 2016;253(8):1557–64.

[29] Lakes RS, Benedict RL. Noncentrosymmetry in micropolar elasticity. Int J Eng Sci 1982;20(10):1161–7.

[30] Papanicolopulos SA. Chirality in isotropic linear gradient elasticity. Int J Solids Struct 2011;48(5):745–52.

[31] Helfrich W, Prost J. Intrinsic bending force in anisotropic membranes made of chiral molecules. Phys Rev A 1988;38(6):3065–8.

[32] Joumaa H, Ostoja-Starzewski M, Ostoja-Starzewski M. Stress and couple-stress invariance in non-centrosymmetric micropolar planar elasticity. P Roy Soc A Math Phys 2011;467(2134):2896–911.

[33] Wang JS, Shimada T, Wang GF, Kitamura T. Effects of chirality and surface stresses on the bending and buckling of chiral nanowires. J Phys D 2013;47(1):015302.

[34] Zhao W, Liu LW, Lan X, Leng JS, Liu YJ. Adaptive repair device concept with shape memory polymer. Smart Mater Struct 2017;26:025027.

[35] Zhao W, Wang Q, Liu LW, Zhu LH, Leng JS, Liu YJ. Structural response measurement of shape memory polymer components using digital image correlation method. Opt Laser Eng 2018;110:323–40.

[36] Zhao W, Liu LW, Zhang FH, Leng JS, Liu YJ. Shape memory polymers and their composites in biomedical applications. Mater Sci Eng C 2019;97:864–83.

[37] Mao Y, Chen F, Hou S, Qi HJ, Yu K. A viscoelastic model for hydrothermally activated malleable covalent network polymer and its application in shape memory analysis. J Mech Phys Solids 2019;127:239–65.

[38] Zhao W, Liu LW, Leng JS, Liu YJ. Thermo-mechanical behavior prediction of carbon nanotube reinforced shape memory polymer composite. Compos Part B 2019;179:107455.

[39] Zhao W, Liu LW, Leng JS, Liu YJ. Thermo-mechanical behavior prediction of shape memory polymer based on the multiplicative decomposition of the deformation gradient. Mech Mater 2020;143:103263.

[40] Xin XZ, Liu LW, Liu YJ, Leng JS. Mechanical models, structures, and applications of shape-memory polymers and their composites. Acta Mech Solida Sin 2019;32:535–65.

[41] Zeng C, Liu LW, Bian WF, Liu YJ, Leng JS. 4D printed electro-induced continuous carbon fiber reinforced shape memory polymer composites with excellent bending resistance. Compos Part B 2020;194:108034.

[42] Zeng CJ, Liu LW, Bian WF, Leng JS, Liu YJ. Compression behavior and energy absorption of 3D printed continuous fiber reinforced composite honeycomb structures with shape memory effects. Addit Manuf 2021;38:101842.

[43] Zhao W, Huang ZP, Liu LW, Wang WB, Leng JS, Liu YJ, et al. Porous bone tissue scaffold concept based on shape memory PLA/Fe$_3$O$_4$. Compos Sci Technol 2021;203:108563.

[44] Briechle K, Hanebeck UD, Proc. SPIE 4387, Optical Pattern Recognition XII, (20 March 2001); https://doi.org/10.1117/12.421129.